doi:10.1093/plcell/koab229

THE PLANT CELL

THE PLANT CELL 2022: 34: 333–350

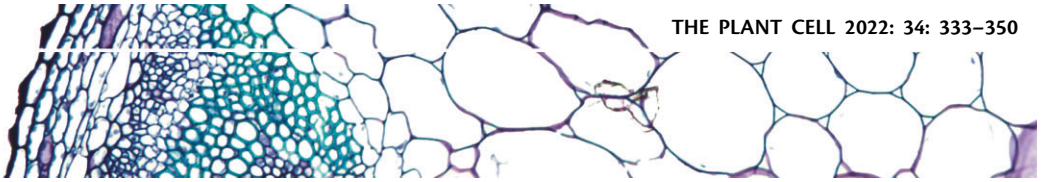

Research Article

COPII Sec23 proteins form isoform-specific endoplasmic reticulum exit sites with differential effects on polarized growth

Mingqin Chang [1,2,†], **Shu-Zon Wu** [1], **Samantha E. Ryken** [1], **Jacquelyn E. O'Sullivan**[3,‡] and **Magdalena Bezanilla** [1,*,§]

1 Department of Biological Sciences, Dartmouth College, Hanover, New Hampshire 03755, USA
2 Plant Biology Graduate Program, University of Massachusetts Amherst, Amherst, Massachusetts 01002, USA
3 Department of Biology, University of Massachusetts Amherst, Amherst, Massachusetts 01002, USA

*Author for correspondence: magdalena.bezanilla@dartmouth.edu
†Present address: Department of Plant Sciences, University of California Davis, Davis, California 95616, USA.
‡Present address: Tufts School of Medicine, Boston, Massachusetts 02111, USA
§Senior author.

M.C. and M.B. designed the research. M.C., S.W., J.E.O., and S.E.R performed the research. M.C., S.W., and M.B. wrote the manuscript.
The author responsible for distribution of materials integral to the findings presented in this article in accordance with the policy described in the Instructions for Authors (https://academic.oup.com/plcell) is: Magdalena Bezanilla (magdalena.bezanilla@dartmouth.edu).

Abstract

Coat Protein complex II (COPII), a coat protein complex that forms vesicles on the endoplasmic reticulum (ER), mediates trafficking to the Golgi. While metazoans have few genes encoding each COPII component, plants have expanded these gene families, leading to the hypothesis that plant COPII has functionally diversified. In the moss *Physcomitrium (Physcomitrella) patens*, the *Sec23/24* gene families are each composed of seven genes. Silencing *Sec23/24* revealed isoform-specific contributions to polarized growth, with the closely related *Sec23D/E* and *Sec24C/D* essential for protonemal development. Focusing on *Sec23*, we discovered that Sec23D/E mediate ER-to Golgi transport and are essential for tip growth, with Sec23D localizing to presumptive ER exit sites. In contrast, *Sec23A*, *B*, *C*, *F*, and *G* are dispensable and do not quantitatively affect ER-to-Golgi trafficking. However, Δ*sec23abcfg* plants exhibited reduced secretion of plasma membrane cargo. Of the four highly expressed protonemal *Sec23* genes, *Sec23F/G* are members of a divergent *Sec23* clade specifically retained in land plants. Notably, Sec23G accumulates on ER-associated foci that are significantly larger, do not overlap with, and are independent of Sec23D. While Sec23D/E form ER exit sites and function as bona fide COPII components essential for tip-growing protonemata, Sec23G and the closely related Sec23F have likely functionally diversified, forming separate and independent ER exit sites and participating in Golgi-independent trafficking pathways.

Introduction

Trafficking from the endoplasmic reticulum (ER) to the Golgi is mediated by Coat Protein complex II (COPII). COPII facilitates the formation of transport vesicles at ER exit sites, promoting the delivery of cargo, including transmembrane proteins, soluble proteins, and lipids, to cis-Golgi compartments (Brandizzi and Barlowe, 2013; Robinson et al., 2015; Barlowe and Helenius, 2016; Aridor, 2018; Hanna et al., 2018). The COPII coat comprises two layers of protein complexes. The inner layer consists of a Sar1-Sec23-Sec24 lattice,

Received August 23, 2021. Accepted September 07, 2021. Advance access publication September 17, 2021

IN A NUTSHELL

Background: Vesicles that form on the endoplasmic reticulum (ER) and are bound for the Golgi apparatus are coated in a complex of proteins known as Coat Protein Complex II (COPII). COPII proteins are highly conserved throughout eukaryotes. Metazoans have few genes encoding each COPII component. By contrast, plants have expanded these gene families. It is unclear if these gene expansions underly increased functional diversification required to pattern and build plant cells.

Question: We wanted to know if the COPII *Sec23* and *Sec24* genes, whose protein products form a dimer and are responsible for cargo sorting as well as recruiting additional coat proteins, have specific contributions to cell growth and patterning.

Findings: Using gene silencing in the model moss species *Physcomitrium patens*, we discovered that individual *Sec23* and *Sec24* genes differentially affect cell growth, with *Sec23D/E* and *Sec24C/D* critical for the development of the tip-growing filamentous tissues in *P. patens*. Focusing on *Sec23*, we analyzed the localization of the three most highly expressed Sec23 proteins in the tip-growing tissues of *P. patens*. Notably, we discovered that Sec23G accumulates on ER-associated foci that are significantly larger, do not overlap with, and are independent of Sec23D. While Sec23D/E form ER exit sites that contribute to secretion that is essential for tip growth, Sec23G and the closely related Sec23F have likely functionally diversified, forming separate and independent ER exit sites. In contrast to Sec23D/E, Sec23F/G do not affect ER-to-Golgi transport, but do affect secretion of proteins to the plasma membrane, suggesting a possible role in Golgi-independent trafficking pathways.

Next steps: Distinct ER exit sites might indicate the formation of COPII coats composed of unique subsets of COPII proteins. Future studies analyzing protein-protein interactions as well as the dependency of localization of each of the COPII proteins will elucidate coat composition and may begin to provide insights into novel trafficking pathways in plants.

while the outer layer is made up of Sec31-Sec13 heterotetramers (Bi et al., 2002; Fath et al., 2007; Stagg et al., 2008; Whittle and Schwartz, 2010). Sar1 is a small GTPase of the Ras super family that is the master regulator of COPII vesicle biogenesis (Nakano and Muramatsu, 1989). The Assembly of the COPII coat is initiated by the conversion of Sar1-GDP to Sar1-GTP, which is mediated by Sec12, a guanine nucleotide exchange factor that is an ER-resident membrane protein (Nakano and Muramatsu, 1989; Barlowe and Schekman, 1993). At the ER surface, activated Sar1 recruits the Sec23-Sec24 heterodimer, which associates with the ER membrane as an "inner coat". The Sar1-Sec23-Sec24-cargo "pre-budding" complex in turn recruits the Sec13-Sec31 heterotetramer, referred to as an "outer coat", to the nascent bud (Salama et al., 1993; Aridor et al., 1998). The polymerization of Sec13-Sec31 heterotetramers induces membrane curvature and completes vesicle biogenesis (Stagg et al., 2006; Fath et al., 2007; Whittle and Schwartz, 2010).

Selective recruitment of cargos into COPII-coated vesicles is driven by ER export signals located on cytoplasmically exposed regions of cargo proteins (Barlowe, 2003). ER export signals of most transmembrane cargo proteins are thought to interact directly with the inner coat components of COPII. However, some transmembrane and most soluble cargo proteins interact with COPII components through ER-resident transmembrane adaptors or receptors (Barlowe, 2003). Sec24 is the COPII component that has been implicated in recognizing these various sorting signals (Mossessova et al., 2003; Nufer, 2003). However, several studies suggested that Sec23 and Sar1 may also play roles in cargo sorting by directly binding to the export signals (Aridor et al., 2001; Giraudo and Maccioni, 2003; Mancias and Goldberg, 2007).

Based on the high sequence similarity among COPII paralogs, and cross-species complementation studies (De Craene et al., 2014; Khoriaty et al., 2018), it has been assumed that the functions of COPII components are conserved across eukaryotes. While components of the COPII coat are well studied in budding yeast and mammalian cells, illustrating their molecular functions in plants has been more challenging. Comparative genomic analyses revealed that gene families encoding COPII components have undergone gene expansions in plants, with *Sec23* exhibiting the largest expansion (Aridor et al., 2001; Giraudo and Maccioni, 2003; Mancias and Goldberg, 2007; Schlacht and Dacks, 2015). While there are only one and two *Sec23* genes in the budding yeast *Saccharomyces cerevisiae* and mammals (e.g. mice and humans; Jensen and Schekman, 2011), respectively, there are seven in both *Physcomitrium (Physcomitrella) patens* and *Arabidopsis thaliana* (Brandizzi, 2018). Since Sec23 and its heterodimeric partner Sec24 are implicated in cargo sorting, the larger *Sec23* gene family could suggest that plants have more diverse sorting signals, requiring specificity at the level of the Sec23/24 heterodimer. Consistent with this notion, in contrast to yeast, which has a single gene for most COPII components, all other components of COPII in plants are encoded by multiple genes, suggesting that cargo specificity may translate to the formation of distinct COPII complexes and vesicle populations. Alternatively, larger gene families could simply indicate that plants have higher functional redundancy in COPII encoded gene families.

Genetic studies in *A. thaliana* have demonstrated that the loss of specific COPII components caused developmental defects. A complete knockout of *AtSec24A* was lethal (Faso et al., 2009; Nakano et al., 2009). However, a missense point mutation in *AtSec24A* (R693K) resulted in ER morphology defects and disruption of ER-Golgi integrity. Interestingly, these phenotypes could not be rescued by either *AtSec24B* or *AtSec24C* (Faso et al., 2009; Nakano et al., 2009), suggesting that *AtSec24B* and *C* are functionally distinct from *AtSec24A*. Even though *AtSec24B* and *AtSec24C* did not rescue the *Atsec24a* missense mutant, and each were not important for plant viability, they were shown to influence the development of reproductive cells (Tanaka et al., 2013). Functional diversification was also suggested by analysis of *AtSec16* mutants, in which storage protein precursors accumulated abnormally in *Atsec16a* null mutants but not in *Atsec16b* null mutants (Takagi et al., 2013).

While *P. patens* and *A. thaliana* have similar numbers of genes encoding COPII components, the moss *P. patens* has several attributes that make it particularly suited to study COPII function. *P. patens* juvenile tissues are haploid and comprise multiple tissue types that establish the plant body. Protonemal tissue, which emerges from the spore and is also readily propagated vegetatively by tissue homogenization, is composed of tip-growing cells constituting a 2D filamentous network. The predictable patterns of growth and cell division provide an easily tractable system for analysis of mutant phenotypes. Protonemal tissue comprises a single-cell layer, which also enables high-resolution microscopy of endogenously tagged fluorescent proteins in live cells (Rensing et al., 2020). In addition to its amenable tissue morphology and haploid lifestyle, *P. patens* is amenable to transient RNA interference for rapid identification of gene function and exhibits high rates of clustered regularly interspaced short palindromic repeats (CRISPR)–Cas9-mediated genome editing (Mallett et al., 2019; Rensing et al., 2020). Here, we utilized these molecular genetic and live-cell imaging tools to systematically characterize the *Sec23* and *Sec24* gene families. Analysis of mutant phenotypes revealed a high degree of functional specificity among Sec23 and Sec24 isoforms. Focusing on the *Sec23* gene family, we discovered that Sec23 isoforms differentially influence ER-to-Golgi trafficking and secretion to the plasma membrane, as well as the size of presumptive ER exit sites.

Results

Sec23 and *Sec24* isoforms differentially affect tip growth

P. patens has seven *Sec23* and seven *Sec24* genes. Based on sequence similarity, there are four subclasses of *Sec23* and *Sec24* genes and in both cases, six of the seven genes exist in closely related pairs (Figure 1, A and B). For *Sec23*, with the exception of *Sec23A*, at least one member of each subclass is highly expressed in protonemal cells (Figure 1A). For *Sec24*, we found that one of the seven *Sec24* genes (*Sec24E*) was not expressed in protonemata (Figure 1B). Of the remaining six genes, *Sec24D* exhibited the lowest expression, while the five other *Sec24* genes were expressed at similar levels (Figure 1B). To determine if *Sec23* and *Sec24* participate in protonemal growth, we used transient RNA interference (RNAi) to silence the *Sec23* and *Sec24* gene families. We used a region of the coding sequence from a member of each subclass (Figure 1, A and B, solid lines under gene models). These sequence regions share a high degree of sequence similarity with the other gene in each subclass (Figure 1, A and B, dashed lines under gene models, Supplemental Table S1) and would effectively simultaneously silence both genes. We did not target *Sec24E* since we were unable to detect a transcript.

By co-transforming the *Sec23G* RNAi construct together with a construct containing the target sequences for *Sec23A*, *C*, and *D*, we targeted the entire *Sec23* gene family and discovered that silencing the seven *Sec23* genes led to a dramatic reduction in growth (Figure 1, C and D; Supplemental File S1). Surprisingly, we found that silencing subclass III genes comprising *Sec23D* and *Sec23E* resulted in a similarly severe growth defect (Figure 1, C and D). In contrast, silencing any of the other subclasses did not affect growth (Figure 1, C and D). These results demonstrate that there is functional specificity among *Sec23* isoforms, with only subclass III playing a critical role in protonemal growth, while the five remaining *Sec23* isoforms do not contribute to protonemal cell expansion.

Similar to silencing subclass III *Sec23* genes, silencing *Sec24C* and *Sec24D* resulted in a 79% reduction in plant area (Figure 1, E and F). Silencing *Sec24F* and *Sec24G* also impaired growth, but to a lesser extent, resulting in a 48% reduction in plant area (Figure 1, E and F). On the other hand, silencing *Sec24A* and *Sec24B* did not affect growth, although both genes were expressed at high levels. These data suggest that like *Sec23* genes, *Sec24* genes differentially contribute to protonemal growth.

Sec23 genes in subclass III are functionally redundant

To test whether *Sec23D* and *Sec23E* within subclass III are functionally redundant, we designed RNAi constructs targeting the untranslated regions (UTRs) of each gene (Figure 2A). Targeting the UTRs of both *Sec23D* and *Sec23E* resulted in small unpolarized plants with an 85% reduction in plant area compared to control RNAi plants (Figure 2, B and C). Silencing *Sec23D* alone resulted in a 59% reduction in plant area, while silencing *Sec23E* did not affect plant area (Figure 2, B and C). Given that *Sec23D* is expressed at a level seven-times higher than *Sec23E* (Figure 1A), it is possible that *Sec23D* contributes to protonemal growth more strongly than *Sec23E*. To test whether *Sec23E* can replace *Sec23D* function if expressed at sufficient levels, we performed complementation studies by driving the full-length coding sequence of *Sec23D* or *Sec23E* with the constitutive maize (*Zea mays*) *Ubiquitin* promoter. Interestingly, the reduction in plant area resulting from silencing of *Sec23D* was

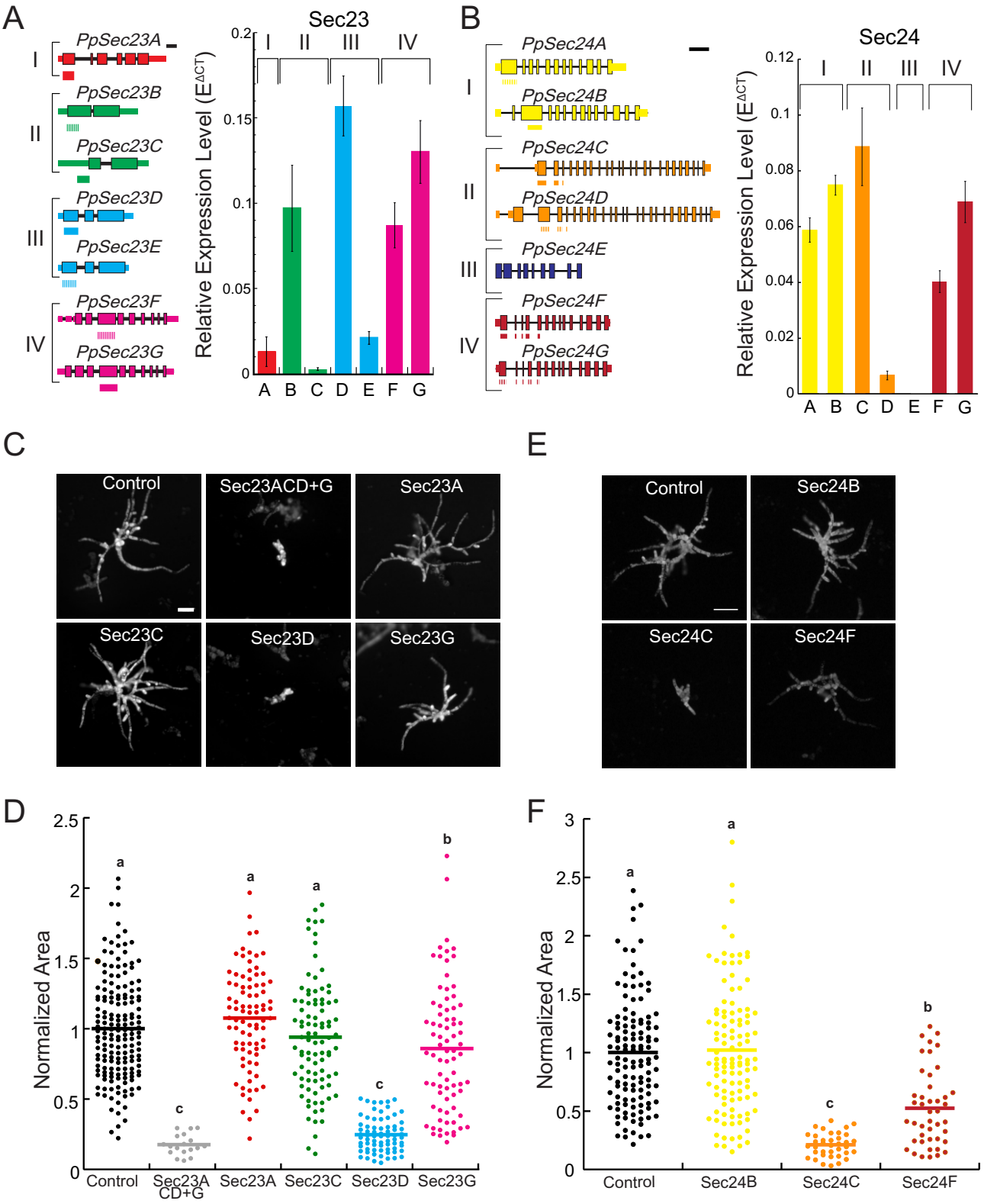

Figure 1 *Sec23* and *Sec24* are required for polarized growth. Gene models of the *P. patens Sec23* (A) and *Sec24* (B) genes are shown with exons indicated by boxes and introns by thin black lines. Coding and untranslated regions are denoted by thick and thin boxes, respectively. The lines underneath the gene models represent sequence regions targeted by the RNAi constructs. Scale bar is 500 bp. Graphs depict the relative expression levels of *Sec23* and *Sec24* genes normalized to *UBIQUITIN10* in 8-day-old wild-type moss plants regenerated from protoplasts. $N = 3$, Error bars are standard error of the mean (SEM). C and E, Representative chlorophyll autofluorescence images of 7-day-old plants regenerated from protoplasts expressing the indicated RNAi constructs. Scale bar, 100 μm. D and F, Quantification of plant area is based on the area of the chlorophyll autofluorescence and is presented normalized to the area of the control for each experiment. Means are indicated by horizontal lines. Letters indicate groups with significantly different means, as determined by a one-way ANOVA with a Tukey's post hoc test ($\alpha = 0.05$).

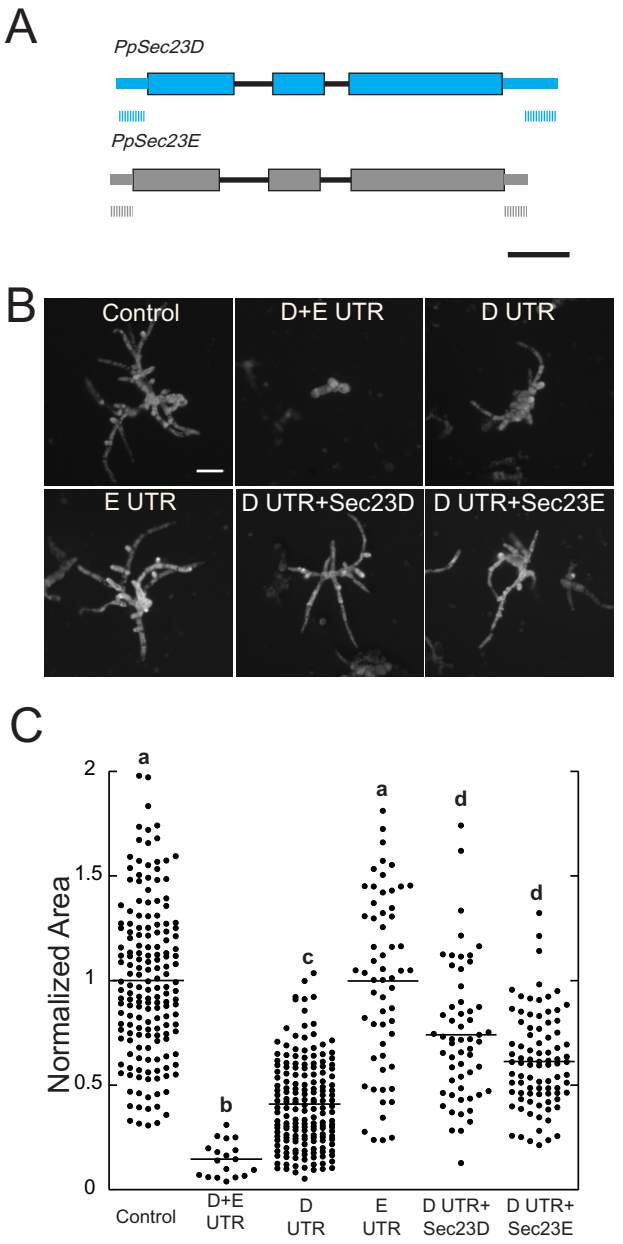

Figure 2 *Sec23D* and *Sec23E* are functionally redundant. A, *Sec23D* and *Sec23E* gene models are shown with exons indicated by boxes and introns by thin black lines. Coding and untranslated regions are denoted by thick and thin boxes, respectively. The lines underneath the gene models represent sequence regions that were targeted by *Sec23D* or *Sec23E* UTR RNAi constructs. Scale bar is 500 bp. B, Representative chlorophyll autofluorescence images of 7-day-old plants regenerated from protoplasts expressing the indicated constructs. Scale bar, 100 µm. C, Quantification of plant area was normalized to the control for each experiment. Letters indicate groups with significantly different means, as determined by a one-way ANOVA with a Tukey's post hoc test ($\alpha = 0.05$).

restored to similar levels when either *Sec23D* or *Sec23E* full-length cDNA was expressed (Figure 2, B and C), indicating that *Sec23D* and *Sec23E* are functionally redundant and that the highly expressed *Sec23D* is the predominant group III isoform critical for protonemal growth.

CRISPR–Cas9-mediated deletion of *Sec23* isoforms

Using transient RNAi, we were able to deduce that *Sec23* genes display isoform-specific functions during protonemal growth. However, transient RNAi assays are limited to phenotypic characterization of 7-day-old plants. To further analyze the molecular functions of *Sec23*, we generated stable loss-of-function mutants of *Sec23* genes using CRISPR–Cas9-mediated genome editing. We targeted each gene with one protospacer located in the first coding exon (Supplemental Figures S1A and S2). We obtained single and higher-order mutants of *Sec23* genes carrying out-of-frame mutations resulting in premature stop codons in their transcripts (Supplemental Figures S1A and S2 and Supplemental Table S2). Consistent with the RNAi results, 7-day-old Δ*sec23d* plants were 70% smaller than wild-type plants, while Δ*sec23e* plants exhibited no growth defects (Figure 3, A and B). We isolated a number of *sec23d* null alleles (Supplemental Figure S1A and Supplemental Table S2), which had similar growth phenotypes (Supplemental Figure S1B). We also found that in 3-week-old plants regenerated from protoplasts, Δ*sec23d-5* plants were 62.6% smaller than the wild-type (Figure 3, C and D), and Δ*sec23d-5* had fewer gametophores compared to the wild-type (Figure 3, C and E). These results suggest that slow growing protonemal tissues resulted in a developmental delay in the production of gametophores.

Although it was possible to isolate many Δ*sec23d* and Δ*sec23e* single mutants, we were unable to obtain Δ*sec23de* double mutants either by targeting *Sec23D* and *Sec23E* simultaneously or by targeting *Sec23D* in the Δ*sec23e-6* single mutant background. This suggests that deleting both *Sec23D* and *Sec23E* is incompatible with protoplast regeneration, which is consistent with the severe growth defects observed by simultaneously silencing *Sec23D* and *Sec23E* using RNAi. Furthermore, we confirmed that none of the other *Sec23* genes were upregulated in Δ*sec23d-5* plants (Supplemental Figure S1C), suggesting that the phenotypic consequences observed were due specifically to the loss of *Sec23D*.

Since the RNAi results suggested that all other *Sec23* subclasses were not required for protonemal growth, we sought to isolate a stable line lacking *Sec23A*, *Sec23B*, *Sec23C*, *Sec23F*, and *Sec23G* to determine if these genes contribute to other aspects of plant growth and development. We successfully isolated two independent quintuple mutant alleles Δ*sec23abcfg-1* and Δ*sec23abcfg-2*, in which *Sec23A*, *Sec23B*, *Sec23C*, *Sec23F*, and *Sec23G* contained lesions resulting in null alleles for each gene (Supplemental Figure S2 and Supplemental Table S2). Most lesions were small deletions or insertions. However, Δ*sec23abcfg-1* contained a 3,000-base pair insertion in the *Sec23G* locus, still resulting in disruption of the *Sec23G* locus (Supplemental Figure S2 and Supplemental Table S2). We characterized both quintuple mutants and found that while 7-day-old Δ*sec23abcfg-1* plants exhibited no detectable growth defects, Δ*sec23abcfg-2* plants exhibited a mild growth defect (Figure 3, B and C). However, 3-week-old Δ*sec23abcfg-1* plants were larger than the wild-type, and Δ*sec23abcfg-2*

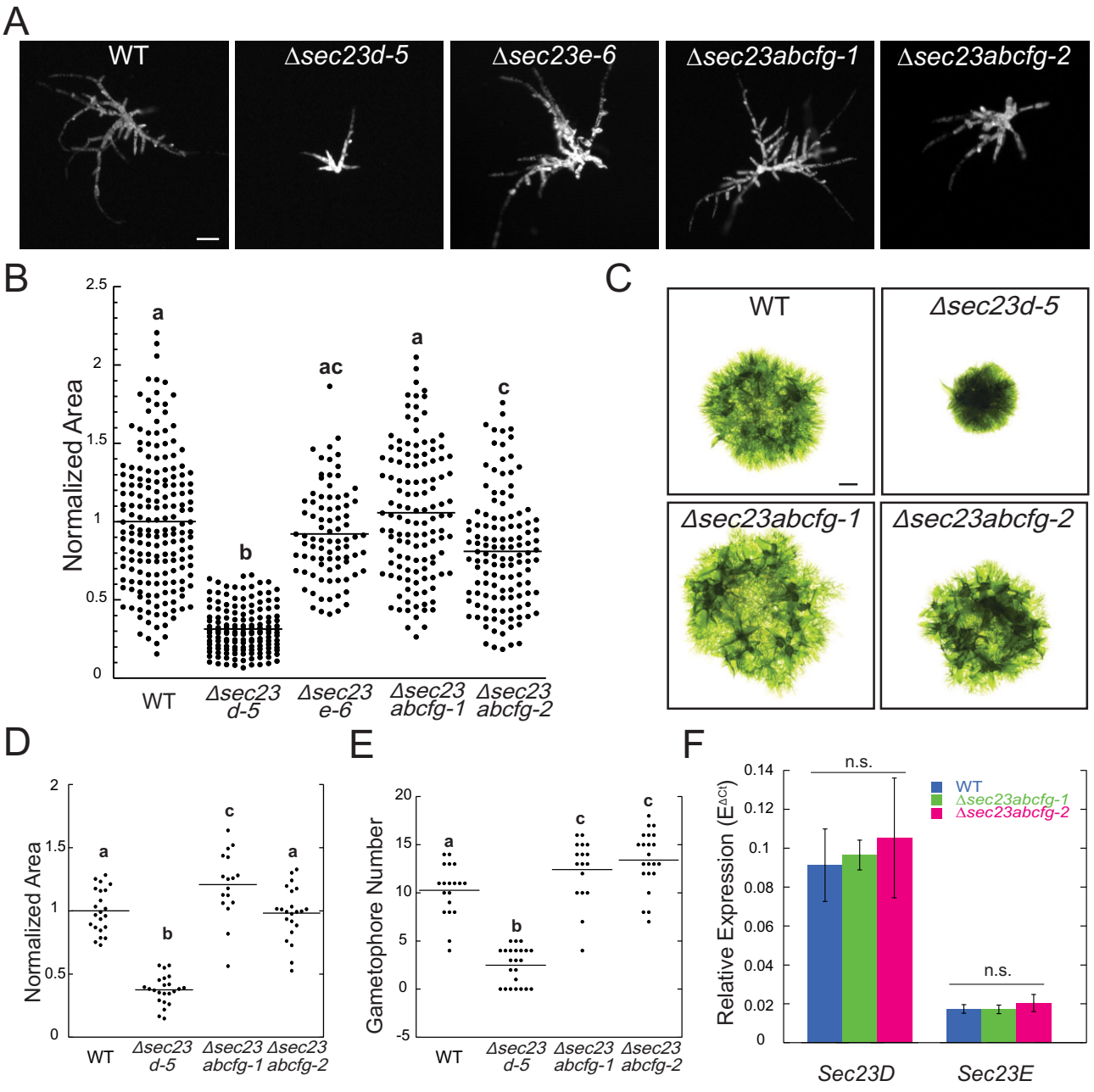

Figure 3 CRISPR-Cas9-mediated deletion of *Sec23* isoforms demonstrates that *Sec23D* is critical for protonemal growth. A, Representative chlorophyll autofluorescence images of 7-day-old plants with the indicated genotype regenerated from protoplasts. Scale bar, 100 μm. B, Quantification of plant area normalized to the wild-type control. C, Representative 3-week-old moss plants with the indicated genotype. Scale bar, 1 mm. D, Quantification of the plant area of 3-week-old moss plants normalized to that of the wild-type control. E, Number of gametophores in 3-week-old moss plants. Letters in (B, D–E) indicate groups with significantly different means, as determined by a one-way ANOVA with a Tukey's post hoc test ($\alpha = 0.05$). F, Relative expression of *Sec23D* and *E* genes normalized to *UBIQUITIN10* in 8-day-old wild-type and Δ*sec23abcfg-1*, and Δ*sec23abcfg-2* moss plants regenerated from protoplasts. $N = 3$, Error bars are SEM. No significant difference (n.s.) was determined by a one-way ANOVA with a Tukey's post hoc test ($\alpha = 0.05$).

plants were indistinguishable from the wild-type (Figure 3, D and E). Interestingly, both Δ*sec23abcfg-1* and Δ*sec23abcfg-2* developed more gametophores than the wild-type (Figure 3E), suggesting that these five *Sec23* genes may negatively regulate gametophore development.

Even though the two quintuple mutant isolates exhibited statistically significant differences at distinct times in development between each other and the wild-type, these were minor compared to the differences between the wild-type and all isolated Δ*sec23d* null mutants. To investigate whether the observed differences might result from differential upregulation of *Sec23D* or *Sec23E* in the Δ*sec23abcfg* mutants, thereby compensating for the loss of *Sec23ABCFG* functions, we measured the expression levels of *Sec23D* and

Sec23E transcripts in Δ*sec23abcfg-1*, Δ*sec23abcfg-2*, and the wild-type. In 8-day-old plants, neither *Sec23D* nor *Sec23E* transcript levels were elevated compared to expression in the wild-type (Figure 3F), indicating that the minor differences observed between the two quintuple mutants were not readily explained by increased expression of either *Sec23D* or *E*. Taken together, the phenotypic analyses of stable *sec23* null plants suggested that *Sec23A*, *B*, *C*, *F*, and *G* do not contribute substantially to the establishment of juvenile moss tissues under laboratory growth conditions. In contrast, *Sec23D* and *E* are essential for this process.

Loss of Sec23D causes ER morphology defects and ER stress

As a predicted member of the COPII complex, Sec23D likely mediates ER-to-Golgi transport. However, it is unclear whether the Δ*sec23d* growth defect is a result of a general impairment of ER-to-Golgi transport or the lack of specific cargo sorted by Sec23D needed for protonemal growth. Studies in other organisms have shown that blocking COPII function alters ER morphology (Novick et al., 1980) and results in elevated levels of unfolded proteins in the ER, leading to activation of the ER unfolded protein response (Belden, 2001; Chung et al., 2016). To analyze Sec23D's function in ER-to-Golgi transport, we investigated whether the loss of Sec23D affects ER morphology and the ER unfolded protein response. We used CRISPR–Cas9-mediated genome editing to knock out Sec23D in a line where the ER is fluorescently labeled by targeting GFP to the ER lumen (Supplemental Figure S1 and Supplemental Table S2). When imaged with a confocal microscope, Δ*sec23d-B11* cells exhibited numerous ER dots (Figure 4A, red and cyan boxes), and 65% of protonemal filaments contained large ER aggregates (Figure 4A, green and yellow boxes). Imaging with a super resolution spinning disc confocal system allowed closer inspection of these aggregates (Figure 4B). Smaller aggregates were clearly composed of accumulated tubules, while large aggregates appeared to have tubules that wrapped around each other (Figure 4B, Movie 1).

If changes in ER morphology result from defective secretion at ER exit sites, then proteins may be inadvertently accumulating in the ER, resulting in upregulation of the unfolded protein response. To test this, we analyzed the expression of an ER heat shock protein Binding immunoglobulin Protein (Bip), which is a well-known ER stress reporter in *A. thaliana* (Noh et al., 2003; Srivastava et al., 2013; Maruyama et al., 2014; Cho and Kanehara, 2017). *P. patens* has two *Bip* paralogs, *Bip1* and *Bip2*. Since *Bip2* expression is low in protonemal tissue (Ortiz-Ramírez et al., 2017), we tested whether *Bip1* is affected under conditions that induce ER stress. Brefeldin A (BFA) inhibits protein secretion by disrupting ER–Golgi integrity (Nebenfuhr, 2002; Niu et al., 2005). We found that after a 24-h BFA treatment, the expression of *Bip1* increased by approximately two-fold (Figure 4C), indicating that *Bip1* is a plausible ER stress reporter in *P. patens*. Interestingly, *Bip1* expression increased five-fold in Δ*sec23d* compared to the wild-type (Figure 4D), demonstrating that Δ*sec23d* suffers from severe ER stress. In contrast, Δ*sec23abcfg-1*, which did not exhibit significant growth defects, had normal levels of *Bip1* expression (Figure 4D) and normal ER morphology (Figure 4A).

Disrupting Sec23D results in reduced ER-to-Golgi trafficking and secretion to the plasma membrane

The ER morphology defects and elevated ER stress in Δ*sec23d* suggest that the transport of secretory cargos might be blocked in this mutant. We reasoned that proteins destined for the Golgi and the plasma membrane would accumulate in the ER in mutants with impaired ER-to-Golgi transport. To test this, we disrupted *Sec23D* in lines that either express Yellow Fluorescent Protein (YFP) fused to the first 49 amino acids of the soybean (*Glycine max*) α-1,2-mannosidase, a Golgi resident protein (YFP-MAN; Nelson et al., 2007; Furt et al., 2012) or an mCherry fusion of a transmembrane protein (F-SNAP-mCherry) previously used to measure exocytosis (van Gisbergen et al., 2018;Supplemental Figure S1 and Supplemental Table S2). Since it would have been time-consuming to regenerate quintuple mutants in these two backgrounds, we instead transformed the YFP-MAN and F-SNAP-mCherry markers into Δ*sec23abcfg-1* plants. We selected lines that had similar expression levels to control lines by measuring the total amount of fluorescence in cells.

In control YFP-MAN lines, YFP signal accumulated in the Golgi, with very little fluorescence observed in the rest of the cell (Figure 5A). In contrast to Δ*sec23d-F12*, while YFP fluorescence still accumulated in the Golgi, a large portion of the fluorescent signal that was presumably retained in the ER was observed diffusely throughout the cell (Figure 5A). To quantify ER-to-Golgi trafficking efficiency, we calculated the fluorescence intensity ratio of the signal in the Golgi divided by the signal in the cytoplasm. A high ratio value indicates efficient delivery to the Golgi, as observed in the control lines (Figure 5B). In contrast, Δ*sec23d-F12* exhibited a significantly lower fluorescence intensity ratio (Figure 5B), indicating that the loss of Sec23D impairs delivery of YFP-MAN to the Golgi. Imaging of Δ*sec23abcfg-1* YFP-MAN and its control line revealed that the majority of the YFP signal localizes to the Golgi, with the Golgi-to-cytoplasm ratios in Δ*sec23abcfg*-1 indistinguishable from the control (Figure 5B), suggesting that trafficking of YFP-MAN to the Golgi is not affected in the quintuple mutant.

Many proteins transported in COPII-coated vesicles ultimately reside at the plasma membrane, are secreted, or are trafficked to the vacuole. Without a fluorescent vacuolar cargo in hand, we instead investigated vacuolar morphology by staining the vacuole with MDY-64, a dye that stains the tonoplast in living plant cells (Scheuring et al., 2015). While we found that vacuolar morphology was similar between the wild-type, Δ*sec23d-5*, and Δ*sec23abcfg-1* plants

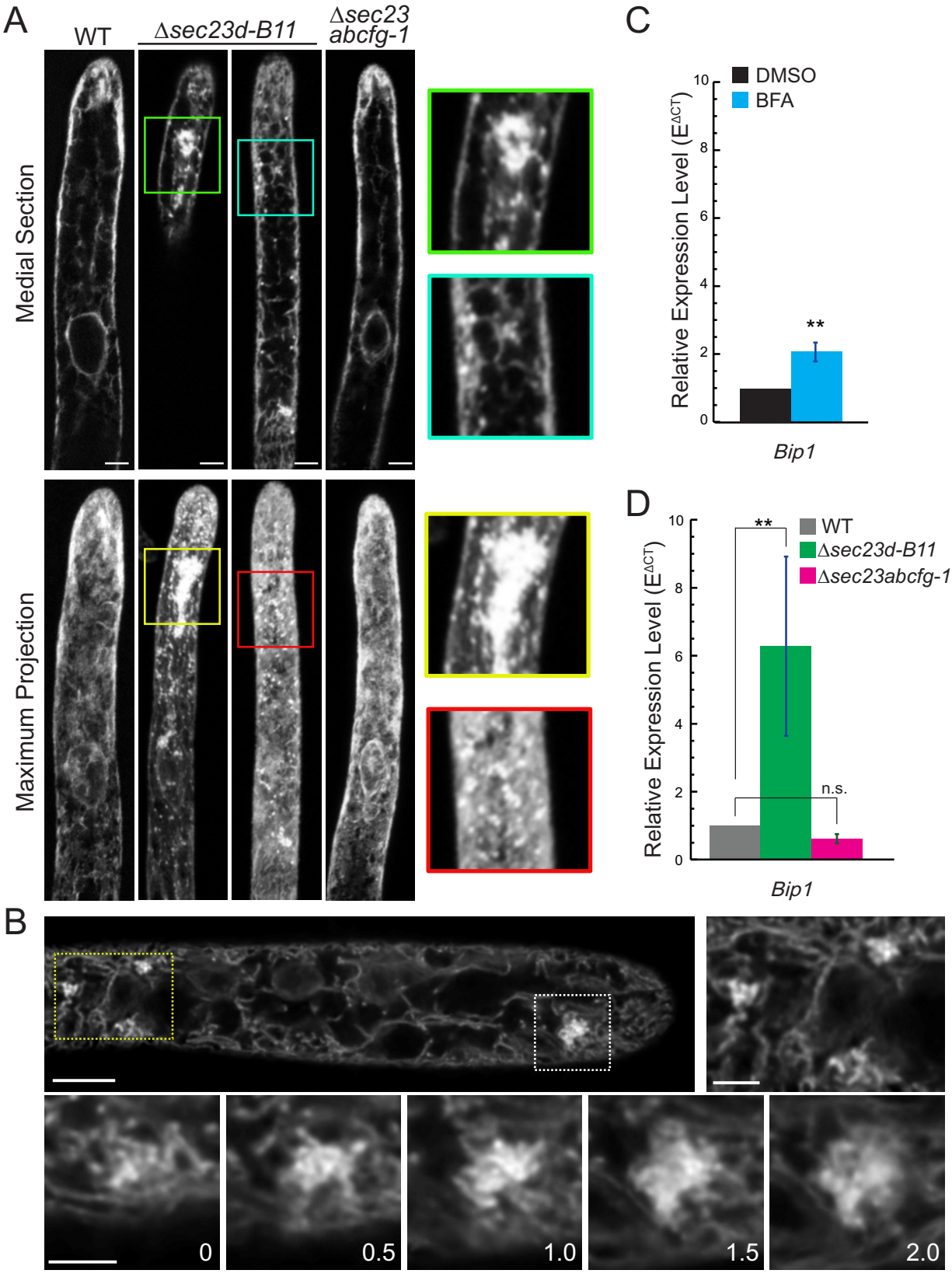

Figure 4 Loss of Sec23D causes ER morphology defects and ER stress. A, Laser scanning confocal images of the ER labeled with GFP-KDEL in the indicated genotype. Colored boxes highlight large and small ER aggregates found in the Δ*sec23d-B11* mutant. Scale bars, 5 μm. B, Spinning disc confocal super resolution imaging of the ER labeled with GFP-KDEL in a Δ*sec23d-B11* cell. Scale bar, 5 μm. The box outlined with a yellow dotted line is enlarged to the right, and the box outlined with a white dotted line is enlarged below, with optical sections spaced every 0.5 μm shown for this region of the cell. Scale bars in boxed regions, 2 μm. Also see Movie 1. C and D, Relative expression of *PpBip1* in 8-day-old moss plants regenerated from protoplasts. $N = 3$, Error bars are SEM. Asterisks denote *t*-probability < 0.01. n.s. denotes no significant difference. In (B), BFA-treated plants were normalized to DMSO-treated plants and in (C), null mutants were normalized to wild-type plants.

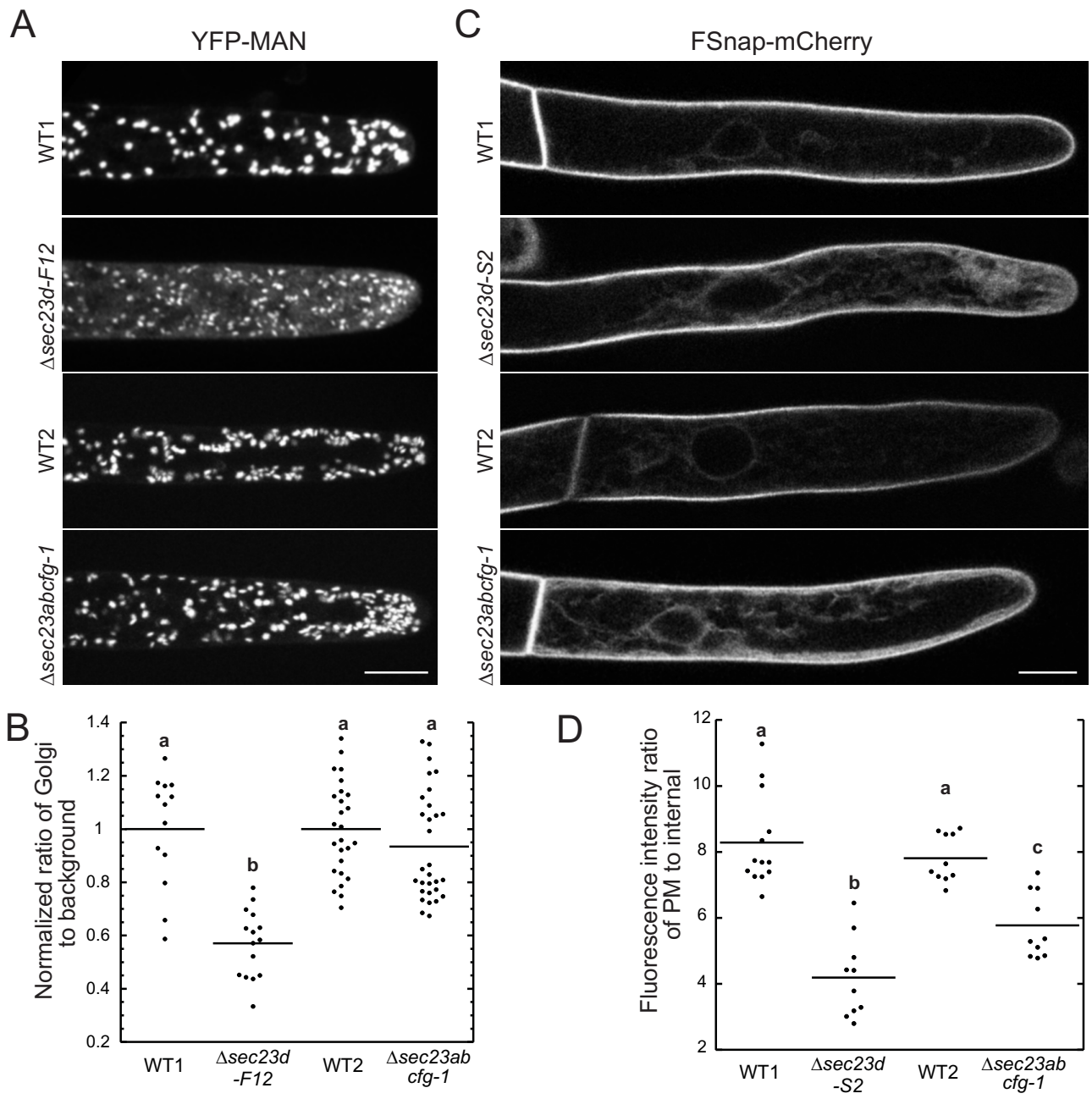

Figure 5 Deletion of *Sec23D* inhibits Golgi trafficking and secretion to the plasma membrane. A, Representative maximum projections of confocal images of the indicated genotypes expressing a YFP-MAN marker. Scale bar, 10 μm. B, Quantification of the fluorescence intensity ratio within the Golgi to the intensity within the cell. C, Representative medial sections of confocal images of the indicated genotypes expressing a plasma membrane marker (FSnap-mCherry). Scale bar, 10 μm. D, Quantification of the fluorescence intensity ratio of the plasma membrane to the intensity within the cell. Letters in (B and D) indicate groups with significantly different means, as determined by a one-way ANOVA with a Tukey's post hoc test ($\alpha = 0.05$).

(Supplemental Figure S3), we cannot rule out the possibility that vacuolar protein sorting has not been affected.

To investigate trafficking to the plasma membrane, we used an engineered fluorescent protein cargo, F-SNAP-mCherry, previously used to analyze exocytosis in protonemata (van Gisbergen et al., 2018). In wild-type cells, F-SNAP-mCherry accumulated on the plasma membrane, with only a very small amount of fluorescence detected inside the cell (Figure 5C). In Δ*sec23d-S2*, a large portion of the mCherry signal was retained in the cell, labeling the ER network (Figure 5C). To quantify secretion efficiency to the plasma membrane, we calculated the fluorescence intensity ratio of the plasma membrane to the intensity within the cell. The ratio in Δ*sec23d-S2* was significantly lower than that of its control line (Figure 5D), indicating that the loss of Sec23D inhibits the secretion of plasma membrane proteins.

Interestingly, we found that the F-SNAP-mCherry signal was also retained inside the cell in the Δ*sec23abcfg-1* mutant, readily observing labeling of the ER network (Figure 5C). In addition, the fluorescence intensity ratio in Δ*sec23abcfg-1* was lower compared to the ratio in its control line (Figure 5D). However, the ratio in Δ*sec23abcfg-1* was still significantly higher than the ratio in Δ*sec23d-S2*, suggesting that secretion of plasma membrane proteins is impaired in Δ*sec23abcfg-1* but to a lesser extent than in Δ*sec23d-S2*. These data, together with the lack of a growth defect in protonemata in the Δ*sec23abcfg-1* mutant, suggest that Sec23A, B, C, F, and G contribute to protein secretion, particularly to the plasma membrane, but importantly, their cargos are not essential for polarized growth in protonemata.

Loss of Sec23D does not affect the cytoskeleton during tip growth

To investigate if defects in protein secretion altered the cytoskeleton, which is critical for polarized expansion in protonemata, we imaged microtubules and actin in the wild-type and in cells carrying null mutations in *Sec23D*. Microtubules align along the length of the cell with their plus ends focused just below the cell apex (Hiwatashi et al., 2014), where a dynamic cluster of actin filaments forms, predicting the site of cell expansion (Wu et al., 2018). Wild-type and Δ*sec23d-M4* cells expressing GFP-tubulin exhibit indistinguishable microtubule networks and both have a focal point of microtubules near the cell tip (Supplemental Figure S4A, arrows). Using Lifeact-mCherry to label the actin network, we found that both the wild-type and Δ*sec23d-5* cells form an apical actin cluster that associates with the growing tip (Supplemental Figure S4B). Time-lapse imaging revealed no discernable differences in the dynamics of the apical actin cluster between the wild-type and Δ*sec23d-5* (Supplemental Figure S4C; Movie 2). These data suggest that tip growth defects in cells lacking Sec23D are independent of the cytoskeleton.

Sec23 isoforms localize to discrete foci associated with the ER

If Sec23 is a bona fide COPII component, we would expect that Sec23 isoforms should associate with the ER. To test this, we inserted sequences in the genome of a line expressing GFP in the ER lumen encoding three tandem mRuby2 red fluorescent proteins (hereafter, 3XmRuby) in-frame with the coding sequences of the three mostly highly expressed protonemal *Sec23* genes: *Sec23B*, *Sec23D*, and *Sec23G* (Figure 1B; Supplemental Figure S5, A and B). To ensure that tagging *Sec23D* did not affect its function, we measured plant area from 7-day-old regenerated protoplasts and found that *Sec23D-3XmRuby* grew indistinguishably from the control lines (Supplemental Figure S5C), suggesting that Sec23D-3XmRuby is functional. By analogy, we reasoned that tagged Sec23B and G would also be functional. To ensure we did not observe any possible dominant negative impacts as a result of the tagging, we performed growth assays of 7-day-old plants regenerated from protoplasts and observed that *Sec23B-3XmRuby* was indistinguishable from the control and *Sec23G-3XmRuby* was slightly smaller (Supplemental Figure S5C).

Confocal microscopy imaging revealed that Sec23D, Sec23B, and Sec23G localized to punctate structures throughout the cytoplasm (Figure 6A). All three proteins labeled foci that were often proximal to the ER (Figure 6A). Co-localization measurements using Pearson's Correlation Coefficient suggested that Sec23D, B, and G foci positively correlated with the ER. To ensure that this correlation was significant, we flipped the ER image both vertically and horizontally and repeated the correlation analysis and found that the correlation coefficients were significantly lower (Figure 6B). Interestingly, Sec23G-3XmRuby foci were larger than the punctate structures found in Sec23D- and Sec23B-3XmRuby lines (Figure 6, A and C). To quantify possible size differences, we imaged all three tagged Sec23 isoforms with a pixel size that maximizes the resolving capacity of the imaging system (Figure 6C, see "Materials and methods") and utilized a segmentation tool in Fiji that identifies particles in the images (Gilles et al., 2017). We discovered that Sec23G particles were significantly larger than Sec23B and D particles. Furthermore, Sec23D particles were slightly larger than Sec23B particles. These data suggest that Sec23 isoforms form distinct compartments on the ER.

Sec23B and Sec23G localization is independent of Sec23D

To further probe the nature of the Sec23 particles, we analyzed the localizations of Sec23B and Sec23G with respect to Sec23D. We used CRISPR–Cas9-mediated homology-directed repair (HDR) to insert sequences encoding mNeonGreen (hereafter, mNeon) in-frame with Sec23B or Sec23G in a Sec23D line endogenously tagged with a single mRuby2 (hereafter, mRuby; Supplemental Figure S6). As expected, Sec23B-mNeon formed small foci, whereas Sec23G-mNeon formed larger foci (Figure 7, A and B). Imaging of Sec23B-mNeon and Sec23D-mRuby revealed the presence of a distribution of cytoplasmic foci, some with only Sec23B-mNeon or only Sec23D-mRuby and some with both (Figure 7A). In contrast, Sec23G-mNeon and Sec23D-mRuby were largely nonoverlapping (Figure 7B). To quantify the degree of overlap, we utilized the segmentation tool in Fiji that identifies fluorescent foci and then determines the number of segmented particles that physically overlap (Gilles et al., 2017). We found that 57% of Sec23B-mNeon co-localized with Sec23D-mRuby. In contrast, only 4% of Sec23G-mNeon showed overlap with Sec23D-mRuby (Figure 7C). In addition to identifying co-localizing particles, the tool also measures the center-to-center distance of overlapping particles (Gilles et al., 2017). Sec23G-mNeon and Sec23D-mRuby had a significantly larger center-to-center distance compared to Sec23B-mNeon and Sec23D-mRuby (Figure 7D), suggesting that any overlap between Sec23G and Sec23D was coincidental.

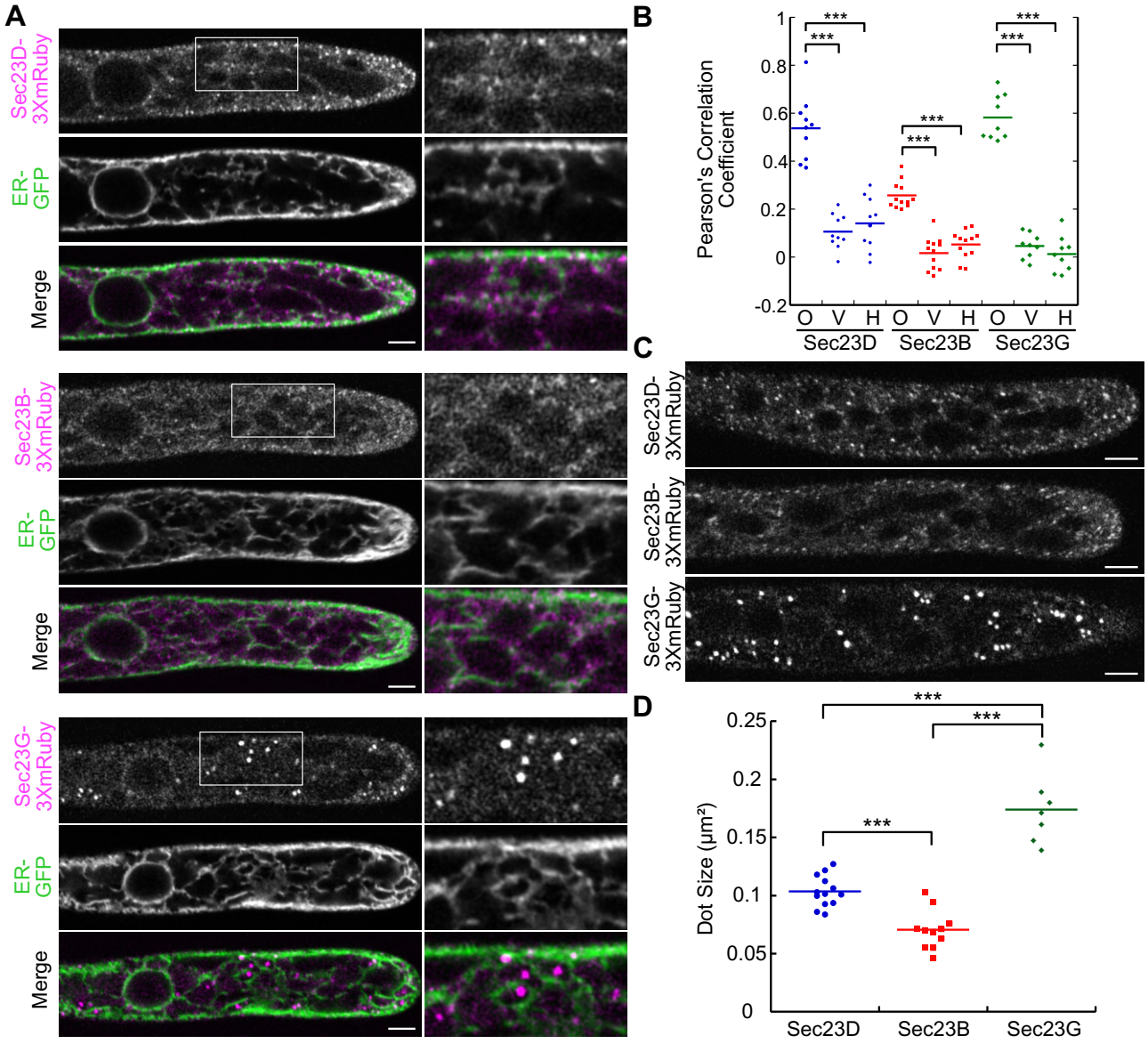

Figure 6 Sec23 isoforms localize to ER proximal structures with distinct sizes. A, Representative confocal Z-sections of lines where the indicated *Sec23* gene was endogenously tagged with 3XmRuby in a line that expresses GFP-KDEL labeling the ER lumen (ER-GFP). Scale bars, 5 µm. Boxed region in the mRuby channel is shown to the right of each image. B, Pearson's correlation coefficient measured between the Sec23 labeled lines and ER-GFP. O, original ER image; V, vertically flipped ER image; H, horizontally flipped ER image. Asterisks denote $P < 0.001$, as determined by a one-way ANOVA with a Tukey's post hoc test ($\alpha = 0.05$). C, Representative confocal Z-sections of *Sec23* genes endogenously tagged with 3XmRuby acquired with the optimal resolution of the confocal imaging system. Scale bars, 5 µm. D, Quantification of average dot size in the Sec23 images, as determined using the diAna tool for Fiji (Gilles et al., 2017). Asterisks denote $P < 0.001$, as determined by a one-way ANOVA with a Tukey post hoc test ($\alpha = 0.05$).

While Sec23B and Sec23D exhibited a high degree of co-localization, COPII vesicles are significantly smaller than the limit of resolution of a light microscope. Therefore, it is unclear if a single vesicle contained both Sec23B and Sec23D or if vesicles formed with a single Sec23 isoform. Given that Sec23G structures are distinct from Sec23D, and 40% of Sec23B and Sec23D foci were not overlapping, we hypothesized that Sec23B, Sec23D, and Sec23G form distinct ER exit sites. If this is the case, we would expect that Sec23B and Sec23G would be unaffected by the loss of Sec23D. Indeed, when we deleted Sec23D in the Sec23B-3XmRuby and Sec23G-3XmRuby lines, both Sec23B and Sec23G still localized to foci (Figure 7E). We quantified the size of these foci and found that Sec23G-3XmRuby was unaffected but Sec23B-3XmRuby was slightly larger in the absence of Sec23D (Figure 7F). However, given that the average Sec23B-3XmRuby particle size is essentially at the limit of resolution of our system, it is unclear how significant this increase may be. Nevertheless, these results demonstrate that even when ER morphology is affected due to the loss of Sec23D, Sec23B, and Sec23G are largely unaffected, suggesting that Sec23B and Sec23G ER exit sites are independent of Sec23D.

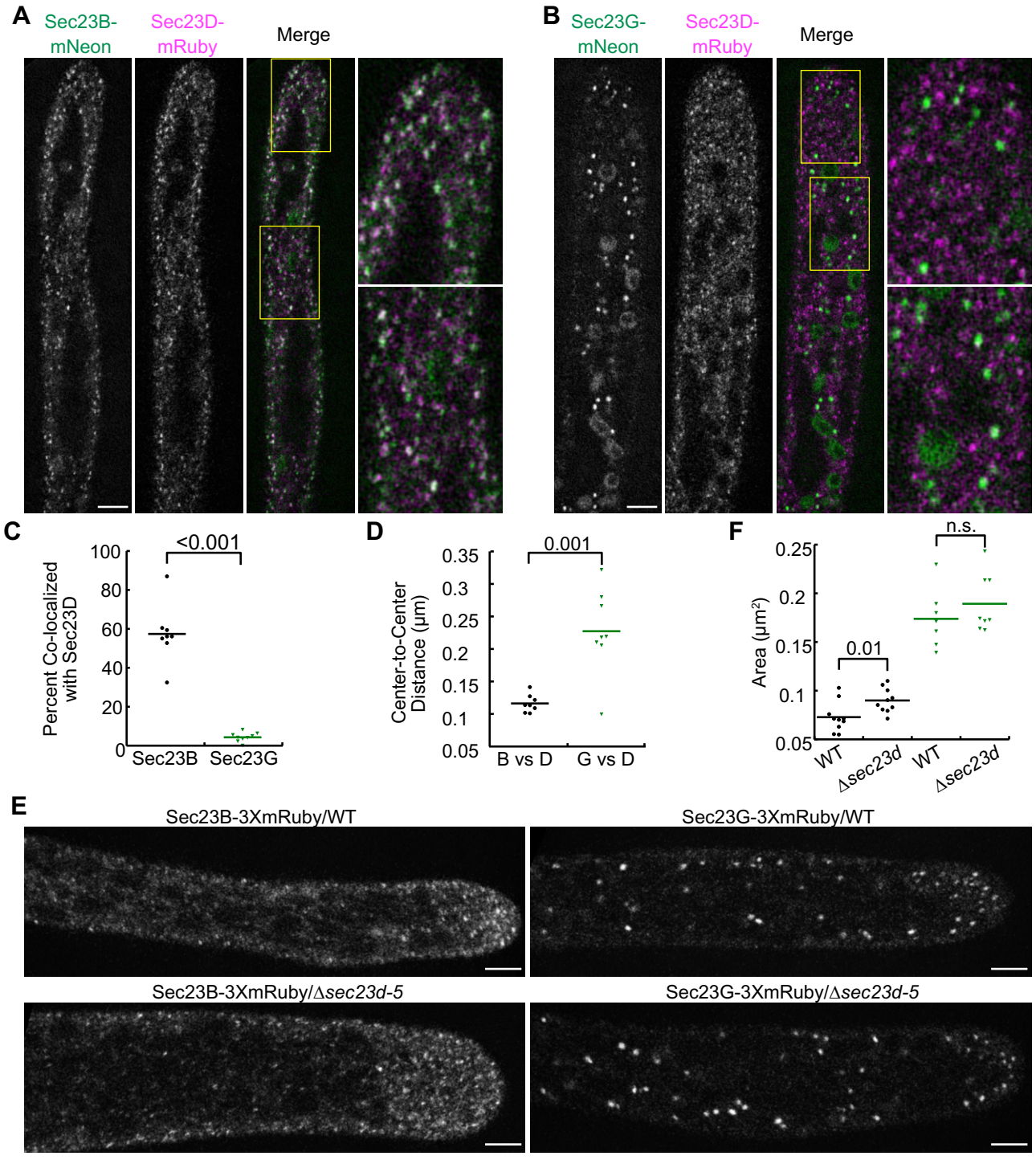

Figure 7 Sec23B and Sec23G form ER-associated foci independent of Sec23D. Representative confocal Z-sections of Sec23D-mRuby lines where Sec23B (A) or Sec23G (B) were endogenously tagged with mNeon. Scale bar, 5 µm. Yellow boxed regions are enlarged to the right of the merged image, where Sec23D-mRuby is false-colored magenta; Sec23B-mNeon is false-colored green in (A), and Sec23G-mNeon is false-colored green in (B). C, Percent of Sec23B-mNeon or Sec23G-mNeon dots that co-localized with Sec23D-mRuby and (D) center-to-center distance of co-localized particles, as determined using the diAna tool for Fiji (Gilles et al., 2017). E, Representative confocal Z-sections of wild-type and Δ*sec23d-5* cells with either Sec23B or Sec23G endogenously tagged with 3XmRuby. Scale bar, 5 µm. F, Quantification of average dot size, as determined using the diAna tool for Fiji (Gilles et al., 2017). Sec23B and Sec23G dot sizes in the wild-type are the same data presented in Figure 6D. Student's *t* test was performed for data in (C, D, and F). The *t*-probability is indicated for each data pair in each graph. n.s. denotes no significant difference.

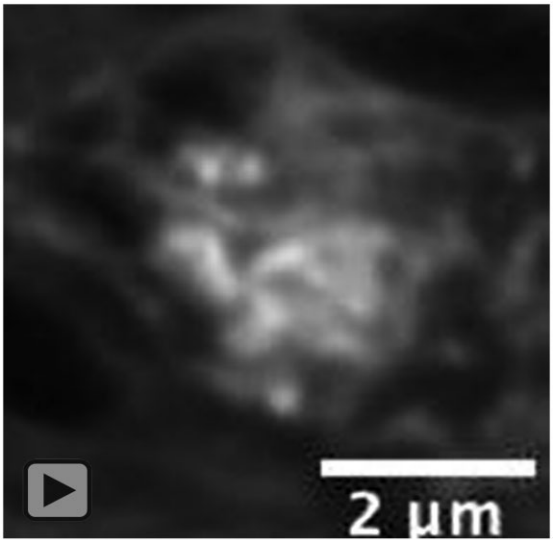

Movie 1 ER tubules aggregate in Δ*sec23d* mutants. Z-sections every 0.5 μm from a super resolution spinning disc confocal Z-stack; see Figure 4B. Movie plays at 5 fps.

Discussion

The large number of genes encoding components of COPII in plants, together with functional studies in Arabidopsis (Faso et al., 2009; Tanaka et al., 2013; De Craene et al., 2014; Chung et al., 2016; Qu et al., 2017; Barlow and Dacks, 2018; Brandizzi, 2018), have led to the hypothesis that gene expansion underlies increased functional diversification required for complex secretory processes that pattern and build plant cells. Evidence suggests that functional diversification could stem from tissue/developmental-specific expression (Lee et al., 2006; Hanton et al., 2009; Hino et al., 2011) or from the formation of COPII complexes composed of specific isoforms with unique functions (Zeng et al., 2015; Zeng et al., 2021). However, it remains unclear whether unique COPII complexes mediate the transport of specific cargos or accumulate at some ER exit sites and not at others. Here, by analyzing the roles of Sec23 and Sec24 isoforms in protonemal development, we have provided evidence for the formation of functionally distinct ER exit sites and the requirement of only Sec23D/E for the transport of cargos uniquely required for tip growth.

We found that Sec23B, Sec23D, and Sec23G all formed foci associated with the ER. However, these foci were distinct. Sec23G dots near the ER were large, whereas Sec23D and Sec23B dots were significantly smaller. Sec23B and Sec23D foci exhibited a high degree of overlap, suggesting that Sec23B and Sec23D may form vesicles in the same region of the ER. In contrast, Sec23G largely did not overlap with Sec23D and by extension likely not Sec23B. The formation of larger domains on the ER suggests that Sec23G may be involved in the secretion of bigger cargo and provides evidence that moss has morphologically distinct ER exit sites that can form, even when ER morphology is disrupted, independently of Sec23D. Given that the loss of Sec23D

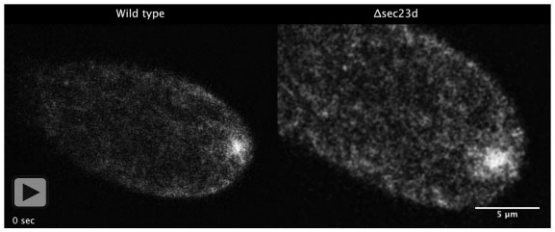

Movie 2 Actin dynamics are not altered in Δsec23d cells. Single focal plane images from a time-lapse acquisition of the wild-type and Δ*sec23d* cells labeled with Lifeact-mCherry. Movie plays at 5 fps.

dramatically reduced ER-to-Golgi transport, while the loss of Sec23A, B, C, F, and G only affected protein secretion to the plasma membrane, our data support the hypothesis that Sec23 isoforms form distinct ER exit sites with differential effects on protein trafficking and growth.

Like *Sec23* isoforms, *Sec24* isoforms also differentially affected protonemal growth. Interestingly, silencing *Sec23D/E* or *Sec24C/D* similarly inhibited tip growth, suggesting that Sec23D/E may heterodimerize with Sec24C/D. *Sec24F/G* also exhibited reduced growth. Thus, it is possible that a number of heterodimer pairs may form that are critical for polarized growth. If this is the case, this suggests that isoform specificity regulates COPII function, which is similar to the finding in Arabidopsis that Sar1A and Sec23A form a unique interaction that mediates functional specificity (Zeng et al., 2015).

Focusing on *Sec23*, where one of the Sec23 pairs, Sec23D/E, plays an essential role in protonemal growth, our data indicate that Sec23D and Sec23E function as bona fide COPII components, with Sec23D expressed at higher levels than E and thereby contributing more to COPII function. While the growth of Δ*sec23d* protonemal cells was significantly slower than that of the wild-type, leading to smaller plants, we were unable to identify any defects in either the actin or microtubule cytoskeletons, suggesting that Sec23D contributes to polarized cell expansion independently of the cytoskeleton. In fact, tip growth in Δ*sec23d* resembles the recently identified *P. patens* Δ*sabre* mutant plants (Cheng and Bezanilla, 2021). SABRE associates with regions of the ER, and its absence has no effect on the cytoskeleton but rather affects the ER, which accumulates aggregates that can be labeled with an ER lumenal marker (Cheng and Bezanilla, 2021). Taken together, these data suggest that abrogated ER function affects polarized growth without altering cytoskeletal organization and dynamics.

Given that Sec23D contributes to ER-to-Golgi transport and secretion to the plasma membrane, while Sec23A, B, C, F, and G contribute to plasma membrane secretion, it is plausible that tip growth requires intact ER-to-Golgi trafficking. In Δ*sec23d* plants, cargos essential for tip growth are either inefficiently carried from the ER to the Golgi or are not properly processed in the Golgi due to severe reductions in trafficking to the Golgi. Perhaps, there is a larger burden for carbohydrates synthesized by enzymes in the Golgi to generate a tip-growing cell wall compared to a diffusely growing

cell wall. To test this, future studies will focus on identifying cargos that have been differentially affected in Δ*sec23d* versus Δ*sec23abcfg* plants. Comparative mass spectrometry of isolated microsomes and plasma membrane extracts in these mutant backgrounds could be very informative. In addition, quantitatively measuring the secretion of known Golgi-resident carbohydrate biosynthetic enzymes and plasma membrane complexes such as cellulose and callose synthases in these mutants could help to narrow down cargo specificity.

With respect to gametophore formation, Δ*sec23d* develops gametophores late, but once gametophores form they are morphologically normal, suggesting that Sec23D function is specifically required during tip growth. In contrast, we found that the five remaining *Sec23* genes were dispensable for the formation of both protonemata and gametophores. Since we were unable to generate Δ*sec23de* or Δ*sec23abcefg* plants, we cannot distinguish between Sec23E playing a critical role in gametophore formation versus Sec23D or Sec23E acting redundantly with Sec23A, B, C, F, and G. If, however, COPII-dependent ER-to-Golgi transport mediated by Sec23D/E is not required for gametophore formation, future experiments involving the conditional removal of Sec23D/E in Δ*sec23abcfg* plants would be expected to lead to normal gametophore formation, providing an opportunity to identify plant-specific COPII-independent secretion pathways thought to play a role in the transport of tonoplast-resident proteins such as the vacuolar H^+-ATPase VHA-a3 (Viotti et al., 2013).

If Sec23D/E are essential and function as the bona fide COPII components mediating ER-to-Golgi transport, what roles do Sec23A, B, C, F, and G play? One possibility is that all or a subset of the remaining Sec23 genes have functionally diversified and no longer contribute to ER-to-Golgi transport. Several lines of evidence support this hypothesis. First, we showed that unlike Δ*sec23d*, Δ*sec23abcfg* plants did not exhibit ER morphology defects or increased ER stress, both of which are characteristic of cargo backing up in the ER, as is often observed in COPII loss-of-function mutants. Second, we showed that Δ*sec23abcfg* had normal ER-to-Golgi transport but were impaired at delivering plasma-membrane bound cargo. Third, analysis of the evolutionary history of COPII subunits across eukaryotes demonstrated that Sec23F/G are members of a divergent Sec23 clade likely present across the Archaeplastida (Schlacht and Dacks, 2015). Interestingly, Sec23F/G orthologs are present in all plant genomes analyzed (Schlacht and Dacks, 2015), suggesting that Sec23F/G has been specifically retained in plants. Thus, phylogenetic studies coupled with our analysis of Sec23 localization suggest that Sec23F/G may be the Sec23 isoforms that have functionally diversified. Given that Sec23G forms large foci at the ER that are distinct and independent of Sec23D, it is possible that Sec23F/G define a novel trafficking pathway in plants, which potentially bypasses the Golgi (Cheng et al., 2009; Zhang et al., 2011; Ding et al., 2012; Wang et al., 2017).

Taking advantage of the facile molecular genetic manipulation and imaging of moss protonemal development, our study has shown that the expanded *Sec23* gene family in moss is multi-faceted. We found evidence that the *Sec23* gene family exhibits aspects of functional redundancy, differential gene expression, as well as isoform specificity for ER exit site formation, ER-to-Golgi trafficking, and importantly transport of essential cargos required for tip growth. Building upon the tools developed in this study, future studies will be able to characterize the remaining COPII components, thereby providing a complete picture of how gene expansions in COPII have been deployed.

Materials and methods

Expression analyses

To quantify expression of the *Sec23* and *Sec24* gene family members (Supplemental Table S3), as well as *Bip1* (Pp3c10_17310), we isolated total RNA from 8-day old plants (various genotypes, as needed for the particular experiment) regenerated from protoplasts using an RNeasy Plant mini prep kit (Qiagen). cDNA was prepared from 1 μg of total RNA using a SuperScript III reverse transcriptase kit, following the manufacturer's recommendation (Invitrogen). Quantitative real time reverse transcriptase (qRT)-PCR assays were conducted with Luna Universal qPCR Master Mix (New England Biolabs). Primers for qRT-PCR analyses are listed in Supplemental Data Set S1. After confirming that amplification efficiencies (calculated from standard curves) were similar for each set of primers (Supplemental Data Set S1), relative expression levels were calculated, and the expression of *Ubiquitin10* was used for normalization. All experiments had three technical replicates (three amplifications from a single cDNA) and three biological replicates. A biological replicate is defined as cDNA generated from total RNA isolated from 8-day-old protonemal tissue regenerated from protoplasts.

Constructs

The *Sec23* and *Sec24* RNAi constructs were generated by PCR amplification of either the coding sequence or 5′- and 3′-UTR of *Sec23* or *Sec24* from *P. patens* cDNA using primers indicated in Supplemental Data Set S1. PCR fragments were cloned into pENTR-D-TOPO (Invitrogen) following the manufacturer's recommendations, and the resulting vectors were sequenced. The *Sec23ACD*-RNAi and *Sec23* UTR-RNAi constructs were generated by stitching together multiple PCR fragments and then directionally cloned into pENTR-D-TOPO as previously described (Vidali et al., 2007). LR Clonase (Invitrogen) reactions were used to transfer either the coding sequence or 5′- and 3′-UTR sequences into the RNAi vector pUGGi (Bezanilla et al., 2005), generating the *Sec23*-CDSi, *Sec24*-CDSi, and *Sec23*-UTRi constructs, respectively. Restriction enzyme digestion was used to verify these constructs.

Expression constructs were generated by PCR amplifying the *Sec23D* and *Sec23E* coding sequences from *P. patens*

cDNA using a 5′ CACC sequence on the forward primers (Supplemental Data Set S1) for oriented cloning into the pENTR-D-TOPO vector (Invitrogen). LR Clonase (Invitrogen) reactions were used to transfer these coding sequences into pTH-Ubi-Gate vectors (Vidali et al., 2007).

Sec23 tagging constructs were generated by PCR amplifying genomic sequences upstream and downstream of the stop codon for *Sec23D*, *Sec23B*, and *Sec23G* using the primers in Supplemental Data Set S1. For *Sec23D*, we used homologous recombination. The distance between the 5′ and 3′ homology arms was 500 bp, which when inserted correctly, the tagging construct replaces these 500 bp with sequences encoding the fluorescent protein and an antibiotic resistance cassette (Supplemental Figures S5 and S6). Using BP Clonase (Invitrogen), homology arms were transferred into vectors, generating homology arm entry clones. Four-fragment recombination reactions were used to assemble the homology arms, fluorescent protein sequence, and the antibiotic resistance cassette into pGEM-gate (Vidali et al., 2009). For *Sec23B* and *Sec23G* tagging, we used CRISPR–Cas9-mediated HDR. 5′- and 3′-homology arms upstream and downstream of the stop codon, with a distance between these two arms of 38 bp for *Sec23B* and 131bp for *Sec23G*, were PCR amplified from genomic DNA (Supplemental Figures S5 and S6). Using BP Clonase (Invitrogen), homology arms were transferred into vectors, generating homology arm entry clones, as described in Mallett et al. (2019). Three-fragment recombination reactions were used to assemble the homology arms and the fluorescent protein sequence into pGEM-gate. We chose the CRISPR–Cas9 protospacer close to the stop codon.

Protospacers for CRISPR–Cas9-mediated mutagenesis and HDR were designed with CRISPOR online software (crispor.tefor.net; Haeussler et al., 2016). Protospacers were selected with high specificity scores and low off-target frequency. Specific overhang sequences were added to facilitate downstream cloning. Protospacers were synthesized as oligonucleotides (Supplemental Data Set S1) and annealed as described (Mallett et al., 2019). Annealed protospacer fragments were transferred to vectors using Instant Sticky-End Ligation Master Mix (New England Biolabs). *Sec23B* and *G* protospacers designed to tag these genes via HDR as well as *Sec23A*, *D*, and *E* protospacers designed to knock out these genes were ligated into pENTR-PpU6-sgRNA-L1L2 (Mallett et al., 2019). *Sec23B* and *F* protospacers designed to knock out these genes were ligated into pENTR-PpU6-sgRNA-L1L5 (Mallett et al., 2019). Sec23C and G protospacers designed to knockout these genes were ligated into pENTR-PpU6-sgRNA-R5L2 (Mallett et al., 2019). LR Clonase (Invitrogen) was used to assemble the protospacer-containing vectors into pZeo-Cas9-Gate, pMH-Cas9-Gate, or pMK-Cas9-Gate vectors (Mallett et al., 2019), as needed. Two-fragment recombination reactions were used to assemble dual targeting mutagenesis vectors for *Sec23B* and *C*, and for *Sec23F* and *G*. Restriction enzyme digestion and sequencing were used to verify these constructs.

Tissue propagation, transformation, and genotyping

All moss (*P. patens*) lines were propagated weekly by moderate homogenization in water and pipetting onto a permeable cellophane-covered solid medium, as described previously (Wu and Bezanilla, 2014). The tissue was grown at room temperature in Percival growth chambers, under 85 $\mu mol_{photons}/m^2s$ light with long-day conditions. PEG-mediated transformations were performed as previously described to generate stable lines (Wu and Bezanilla, 2014), CRISPR–Cas9 genome edited lines (Mallett et al., 2019), and to perform transient RNAi (Vidali et al., 2007).

To genotype mutants generated by CRISPR–Cas9 mutagenesis, we extracted DNA from plants that were 3–4 weeks old (0.5–1 cm in diameter) using the protocol described in (Augustine et al., 2011). For editing experiments, we used primers (Supplemental Data Set S1) surrounding the expected Cas9 cleavage site (∼300–400 bp on each side). A T7 endonuclease assay was used to screen candidate mutants as described (Mallett et al., 2019). For HDR tagging and homologous recombination tagging, we used primers (Supplemental Data Set S1) outside of the homology region to avoid amplification of residual DNA donor template.

Imaging and morphometric analysis of growth assays

For transient RNAi, complementation analyses, and growth assays of stable lines, plants regenerated from protoplasts were photographed seven days after protoplast regeneration. For transient RNAi and complementation analyses, plants lacking nuclear GFP signal were imaged because these were the plants that were actively silenced as described previously (Bezanilla et al., 2005; Vidali et al., 2007). For growth assays of stable lines, any regenerated plant was imaged. Images were acquired with a 1X objective using a stereomicroscope (Leica MZ16FA or Nikon SMZ25) equipped with a CCD camera (Leica DF300FX or Nikon digital sight DS-Fi2). Chlorophyll fluorescence and any nuclear GFP signal were acquired simultaneously using filters (480/40, dichroic 505 (Leica) or dichroic 510 (Nikon), emission 510 long pass). Exposure settings were maintained constant throughout an experiment. Three-week-old plants regenerated from protoplasts were imaged with white light on a Nikon SMZ25 stereomicroscope equipped with a Nikon digital sight DS-Fi2 color camera.

To quantify plant area, individual plants were cropped from images and the red channel, representing chlorophyll fluorescence of the plant, was separated from the RGB image. Threshold settings were set manually for all plants within an experiment. To quantify brightfield images of 3-week-old plants, the blue channel, representing chlorophyll fluorescence of the plant, was separated from the RGB image and thresholded. Total area was calculated from the largest thresholded object in the selected window. All images analysis was done using macros (Galotto et al., 2019) written for ImageJ. Analysis of variation (ANOVA) for multiple comparisons was performed with KaleidaGraph

(Synergy) using the Tukey HSD post hoc tests. The alpha for statistical significance was set to 0.05.

Laser-scanning confocal microscope imaging and quantification

For imaging Sec23B, D, and G localization and dynamics, 5- to 8-day-old plants regenerated from protoplasts were placed onto an agar pad in Hoagland's buffer (4-mM KNO_3, 2-mM KH_2PO_4, 1-mM $Ca(NO_3)_2$, 89-μM Fe citrate, 300-μM $MgSO_4$, 9.93-μM H_3BO_3, 220-nM $CuSO_4$, 1.966-μM $MnCl_2$, 231-nM $CoCl_2$, 191-nM ZnSO4, 169-nM KI, 103-nM Na_2MoO_4, and 1% sucrose), covered by a glass coverslip, and sealed with VALAP (1:1:1 parts of Vaseline, lanoline, and paraffin). For imaging of ER morphology, Golgi resident protein secretion, and F-SNAP-mCherry secretion, we used microfluidic imaging chambers (Bascom et al., 2016). Ground protonemal tissue was gently pipetted into the central part of the device, followed by an infusion of Hoagland's medium. Then the chamber was submerged in Hoagland's medium and placed under constant 85 $\mu mol_{photons}/m^2s$ light.

Images were acquired on a Nikon A1R confocal microscope system with a 1.49 NA 60X oil immersion objective (Nikon) at room temperature. Image acquisition was controlled by NIS-Element AR 4.1 software (Nikon). Laser illumination at 488 nm was used to excite mNeon, YFP, GFP, and chlorophyll autofluorescence; 561 nm for mRuby, mCherry. Emission filters were 525/50 nm for mNeon, YFP, and GFP; 595/50 nm for mRuby and mCherry.

Super resolution spinning disc confocal imaging was performed with a Nikon CSUW1-SoRA system. Images were acquired with a 60× Plan Apo 1.40NA objective with the 2.8× magnifying lens. Laser illumination at 488 nm was used to excite GFP, and the Emission filters were 525/50. Images were denoised using the denoise.ai machine learning algorithm and deconvolved using the Richardson-Lucy algorithm within NIS-Elements v5.21 software.

To quantify trafficking to the Golgi, confocal Z-stacks of individual cells were converted to a maximum intensity projection. To quantify secretion to the plasma membrane, the medial focal plane was selected for analysis. YFP (YFP-MAN) and mCherry (FSnap-mCherry) fluorescence intensities with the same expression pattern were normalized using enhanced contrast in Fiji. Images were cropped to isolate regions only within the cell. Then, using a minimum threshold of 20,000–22,000, it was possible to isolate and measure the fluorescence intensity of the Golgi structures (Golgi intensity) or the plasma membrane with the analyze particles function in Fiji. The fluorescence intensity of the background was similarly measured using the same threshold cut-off for each image but unchecking dark background, thereby selecting all regions below the threshold cut off. These values were used to calculate the ratio of Golgi/plasma membrane intensity to background intensity. To quantify the Pearson's Correlation Coefficient, we analyzed single focal planes with the Coloc2 plugin in Fiji comparing the original images as well as horizontally and vertically flipped ER-GFP images. To quantify the size and co-localization of Sec23B, D, and G dots, we analyzed single focal planes and used the Distance Analysis (diAna) tool for ImageJ, which uses object-based identification for distance and co-localization measurements (Gilles et al., 2017) and has been recently used to define specific subdomains of the trans Golgi network in plant cells (Heinze et al., 2020). All images were acquired with a pixel size of 0.07 μm and processed by subtracting background, enhancing contrast with normalization, and smoothing in Fiji prior to performing segmentation with diAna. For Sec23G-mNeon, chloroplast autofluorescence was collected in the far-red channel and subtracted from the green channel. To segment the dots in the image, we used the iterative option with a minimum threshold of 25,000–27,500 and a step value of 20. After segmentation in diAna, we obtained the size of all segmented regions, as well the percent of co-localizing particles. For particles that did overlap, we also extracted the center-to-center distance of those overlapping particles. For all data, ANOVA for multiple comparisons was performed with KaleidaGraph (Synergy) using the Tukey's HSD post hoc tests. The alpha for statistical significance was set to 0.05. For pairwise comparisons, a Student's *t* test was used using KaleidaGraph (Synergy).

Accession numbers

Sequence data from this article can be found in the Phytozome database with the gene IDs listed in Supplemental Table S3.

Supplemental data

The following materials are available in the online version of this article.

Supplemental Figure S1. CRISPR–Cas9-mediated editing of *Sec23D* and *Sec23E*.

Supplemental Figure S2. CRISPR–Cas9-mediated editing of *Sec23A*, *B*, *C*, *F*, and *G*.

Supplemental Figure S3. Vacuolar morphology is unaffected in *Sec23* mutant plants.

Supplemental Figure S4. The cytoskeleton is unaffected in Δ*sec23d* plants.

Supplemental Figure S5. Molecular characterization of endogenous tagging of Sec23D, B, and G with 3XmRuby.

Supplemental Figure S6. Molecular characterization of endogenous tagging of Sec23 B and G with mNeon and Sec23D with mRuby.

Supplemental Table S1. Sequence comparisons of the fragments used in the RNAi constructs.

Supplemental Table S2. Mutants used in this study.

Supplemental Table S3. Gene IDs for *Sec23* and *Sec24* gene family members.

Supplemental Data Set S1. Primers used in this study.

Supplemental File S1. ANOVA tables.

Acknowledgments

We thank members of the Bezanilla lab for careful reading of the manuscript. M.C. received support from the Plant Biology

Graduate Program at the University of Massachusetts, Amherst. This work was supported by Dartmouth College and grants from the National Science Foundation (MCB-1330171 and MCB-1715785 to M.B.).

Conflict of interest statement. None declared.

References

Aridor M (2018) COPII gets in shape: lessons derived from morphological aspects of early secretion. Traffic **19:** 823–839

Aridor M, Fish KN, Bannykh S, Weissman J, Roberts TH, Lippincott-Schwartz J, Balch WE (2001) The Sar1 Gtpase coordinates biosynthetic cargo selection with endoplasmic reticulum export site assembly. J Cell Biol **152:** 213–230

Aridor M, Weissman J, Bannykh S, Nuoffer C, Balch WE (1998) Cargo selection by the COPII budding machinery during export from the ER. J Cell Biol **141:** 61–70

Augustine RC, Pattavina KA, Tüzel E, Vidali L, Bezanilla M (2011) Actin interacting protein1 and actin depolymerizing factor drive rapid actin dynamics in Physcomitrella patens. Plant Cell **23:** 3696–3710

Barlow LD, Dacks JB (2018) Seeing the endomembrane system for the trees: evolutionary analysis highlights the importance of plants as models for eukaryotic membrane-trafficking. Semin Cell Dev Biol **80:** 142–152

Barlowe C (2003) Signals for COPII-dependent export from the ER: what's the ticket out? Trends Cell Biol **13:** 295–300

Barlowe C, Helenius A (2016) Cargo capture and bulk flow in the early secretory pathway. Annu Rev Cell Dev Biol **32:** 197–222

Barlowe C, Schekman R (1993) SEC12 encodes a guanine-nucleotide-exchange factor essential for transport vesicle budding from the ER. Nature **365:** 347–349

Bascom CS, Wu S-Z, Nelson K, Oakey J, Bezanilla M (2016) Long-term growth of moss in microfluidic devices enables subcellular studies in development. Plant Physiol **172:** 28–37

Belden WJ (2001) Role of Erv29p in collecting soluble secretory proteins into ER-derived transport vesicles. Science **294:** 1528–1531

Bezanilla M, Perroud P-F, Pan A, Klueh P, Quatrano RS (2005) An RNAi system in Physcomitrella patens with an internal marker for silencing allows for rapid identification of loss of function phenotypes. Plant Biol (Stuttg) **7:** 251–257

Bi X, Corpina RA, Goldberg J (2002) Structure of the Sec23/24–Sar1 pre-budding complex of the COPII vesicle coat. Nature **419:** 271–277

Brandizzi F (2018) Transport from the endoplasmic reticulum to the Golgi in plants: where are we now? Semin Cell Dev Biol **80:** 94–105

Brandizzi F, Barlowe C (2013) Organization of the ER–Golgi interface for membrane traffic control. Nat Rev Mol Cell Biol **14:** 382–392

Cheng F-y, Zamski E, Guo W-w, Mason Pharr D, Williamson JD (2009) Salicylic acid stimulates secretion of the normally symplastic enzyme mannitol dehydrogenase: a possible defense against mannitol-secreting fungal pathogens. Planta **230:** 1093–1103

Cheng X, Bezanilla M (2021) SABRE populates ER domains essential for cell plate maturation and cell expansion influencing cell and tissue patterning. eLife **10:** e65166

Cho Y, Kanehara K (2017) Endoplasmic reticulum stress response in Arabidopsis roots. Front Plant Sci **8**

Chung KP, Zeng Y, Jiang L (2016) COPII paralogs in plants: functional redundancy or diversity? Trends Plant Sci **21:** 758–769

De Craene J-O, Courte F, Rinaldi B, Fitterer C, Herranz MC, Schmitt-Keichinger C, Ritzenthaler C, Friant S (2014) Study of the plant COPII vesicle coat subunits by functional complementation of yeast Saccharomyces cerevisiae mutants. PLoS ONE **9:** e90072

Ding Y, Wang J, Wang J, Stierhof Y-D, Robinson DG, Jiang L (2012) Unconventional protein secretion. Trends Plant Sci **17:** 606–615

Faso C, Chen Y-N, Tamura K, Held M, Zemelis S, Marti L, Saravanan R, Hummel E, Kung L, Miller E, et al. (2009). A missense mutation in the Arabidopsis COPII coat protein Sec24A induces the formation of clusters of the endoplasmic reticulum and Golgi apparatus. Plant Cell **21:** 3655–3671

Fath S, Mancias JD, Bi X, Goldberg J (2007) Structure and organization of coat proteins in the COPII cage. Cell **129:** 1325–1336

Furt F, Lemoi K, Tüzel E, Vidali L (2012) Quantitative analysis of organelle distribution and dynamics in Physcomitrella patens protonemal cells. BMC Plant Biol **12:** 70

Galotto G, Bibeau JP, Vidali L (2019) Automated image acquisition and morphological analysis of cell growth mutants in Physcomitrella patens. Methods Mol Biol 1992: 307–322

Gilles J-F, Dos Santos M, Boudier T, Bolte S, Heck N (2017) DiAna, an ImageJ tool for object-based 3D co-localization and distance analysis. Methods **115:** 55–64

Giraudo CG, Maccioni HJF (2003) Endoplasmic reticulum export of glycosyltransferases depends on interaction of a cytoplasmic dibasic motif with Sar1. MBoC **14:** 3753–3766

van Gisbergen PAC, Wu S-Z, Chang M, Pattavina KA, Bartlett ME, Bezanilla M (2018) An ancient Sec10-formin fusion provides insights into actin-mediated regulation of exocytosis. J Cell Biol **217:** 945–957

Haeussler M, Schönig K, Eckert H, Eschstruth A, Mianné J, Renaud J-B, Schneider-Maunoury S, Shkumatava A, Teboul L, Kent J, et al. (2016). Evaluation of off-target and on-target scoring algorithms and integration into the guide RNA selection tool CRISPOR. Genome Biol **17:** 148

Hanna MG, Peotter JL, Frankel EB, Audhya A (2018) Membrane transport at an organelle interface in the early secretory pathway: take your coat off and stay a while: evolution of the metazoan early secretory pathway. BioEssays **40:** 1800004

Hanton SL, Matheson LA, Chatre L, Brandizzi F (2009) Dynamic organization of COPII coat proteins at endoplasmic reticulum export sites in plant cells. Plant J **57:** 963–974

Heinze L, Freimuth N, Rößling A-K, Hahnke R, Riebschläger S, Fröhlich A, Sampathkumar A, McFarlane HE, Sauer M (2020) EPSIN1 and MTV1 define functionally overlapping but molecularly distinct trans-Golgi network subdomains in Arabidopsis. PNAS **117:** 25880–25889

Hino T, Tanaka Y, Kawamukai M, Nishimura K, Mano S, Nakagawa T (2011) Two Sec13p homologs, AtSec13A and AtSec13B, redundantly contribute to the formation of COPII transport vesicles in *Arabidopsis thaliana*. Biosci Biotechnol Biochem **75:** 1848–1852

Hiwatashi Y, Sato Y, Doonan JH (2014) Kinesins have a dual function in organizing microtubules during both tip growth and cytokinesis in Physcomitrella patens. Plant Cell **26:** 1256–1266

Jensen D, Schekman R (2011) COPII-mediated vesicle formation at a glance. J Cell Sci **124:** 1–4

Khoriaty R, Hesketh GG, Bernard A, Weyand AC, Mellacheruvu D, Zhu G, Hoenerhoff MJ, McGee B, Everett L, Adams EJ, et al. (2018) Functions of the COPII gene paralogs SEC23A and SEC23B are interchangeable in vivo. Proc Natl Acad Sci USA **115:** E7748–E7757

Lee MH, Lee SH, Kim H, Jin JB, Kim DH, Hwang I (2006) A WD40 repeat protein, Arabidopsis Sec13 Homolog 1, may play a role in vacuolar trafficking by controlling the membrane association of AtDRP2A. Mol Cells **22:** 210–219.

Mallett DR, Chang M, Cheng X, Bezanilla M (2019) Efficient and modular CRISPR-Cas9 vector system for Physcomitrella patens. Plant Direct **3:** e00168–15

Mancias JD, Goldberg J (2007) The transport signal on Sec22 for packaging into COPII-coated vesicles is a conformational epitope. Mol Cell **26:** 403–414

Maruyama D, Sugiyama T, Endo T, Nishikawa S (2014) Multiple BiP genes of Arabidopsis thaliana are required for male gametogenesis and pollen competitiveness. Plant Cell Physiol **55:** 801–810

Mossessova E, Bickford LC, Goldberg J (2003) SNARE selectivity of the COPII coat. Cell **114:** 483–495

Nakano A, Muramatsu M (1989) A novel GTP-binding protein, Sarlp, is involved in transport from the endoplasmic reticulum to the Golgi apparatus. J Cell Biol **109:** 2677–2691

Nakano RT, Matsushima R, Ueda H, Tamura K, Shimada T, Li L, Hayashi Y, Kondo M, Nishimura M, Hara-Nishimura I (2009) GNOM-LIKE1/ERMO1 and SEC24a/ERMO2 are required for maintenance of endoplasmic reticulum morphology in Arabidopsis thaliana. Plant Cell **21:** 3672–3685

Nebenfuhr A (2002) Brefeldin A: deciphering an enigmatic inhibitor of secretion. Plant Physiol **130:** 1102–1108

Nelson BK, Cai X, Nebenführ A (2007) A multicolored set of in vivo organelle markers for co-localization studies in Arabidopsis and other plants. Plant J **51:** 1126–1136

Niu T-K, Pfeifer AC, Lippincott-Schwartz J, Jackson CL (2005) Dynamics of GBF1, a Brefeldin A-sensitive Arf1 exchange factor at the Golgi□V. Mol Biol Cell **16:** 1213–1222

Noh S-J, Kwon CS, Oh D-H, Moon JS, Chung W-I (2003) Expression of an evolutionarily distinct novel BiP gene during the unfolded protein response in Arabidopsis thaliana. Gene **311:** 81–91

Novick P, Field C, Schekman R (1980) Identification of 23 complementation groups required for post-translational events in the yeast secretory pathway. Cell **21:** 205–215

Nufer O (2003) ER export of ERGIC-53 is controlled by cooperation of targeting determinants in all three of its domains. J Cell Sci **116:** 4429–4440

Ortiz-Ramírez C, Michard E, Simon AA, Damineli DSC, Hernandez-Coronado M, Becker JD, Feijó JA (2017) GLUTAMATE RECEPTOR-LIKE channels are essential for chemotaxis and reproduction in mosses. Nature **549:** 91–95

Qu X, Zhang R, Zhang M, Diao M, Xue Y, Huang S (2017) Organizational innovation of apical actin filaments drives rapid pollen tube growth and turning. Mol Plant **10:** 930–947

Rensing SA, Goffinet B, Meyberg R, Wu S-Z, Bezanilla M (2020) The moss *Physcomitrium* (*Physcomitrella*) *patens*: a model organism for non-seed plants. Plant Cell **32:** 1361–1376

Robinson DG, Brandizzi F, Hawes C, Nakano A (2015) Vesicles versus tubes: is endoplasmic reticulum-Golgi transport in plants fundamentally different from other eukaryotes? Plant Physiol **168:** 393–406

Salama NR, Yeung T, Schekman RW (1993) The Secl3p complex and reconstitution of vesicle budding from the ER with purified cytosolic proteins. EMBO J **12:** 4073–4082

Scheuring D, Schöller M, Kleine-Vehn J, Löfke C (2015) Vacuolar staining methods in plant cells. Methods Mol Biol **1242:** 83–92

Schlacht A, Dacks JB (2015) Unexpected ancient paralogs and an evolutionary model for the COPII coat complex. Genome Biol Evol **7:** 1098–1109

Srivastava R, Deng Y, Shah S, Rao AG, Howell SH (2013) BINDING PROTEIN is a master regulator of the endoplasmic reticulum stress sensor/transducer bZIP28 in *Arabidopsis*. Plant Cell **25:** 1416–1429

Stagg SM, Gürkan C, Fowler DM, LaPointe P, Foss TR, Potter CS, Carragher B, Balch WE (2006) Structure of the Sec13/31 COPII coat cage. Nature **439:** 234–238

Stagg SM, LaPointe P, Razvi A, Gürkan C, Potter CS, Carragher B, Balch WE (2008) Structural basis for cargo regulation of COPII coat assembly. Cell **134:** 474–484

Takagi J, Renna L, Takahashi H, Koumoto Y, Tamura K, Stefano G, Fukao Y, Kondo M, Nishimura M, Shimada T, et al. (2013). MAIGO5 Functions in Protein Export from Golgi-Associated Endoplasmic Reticulum Exit Sites in Arabidopsis. The Plant Cell **25**: 4658–4675.

Tanaka Y, Nishimura K, Kawamukai M, Oshima A, Nakagawa T (2013) Redundant function of two Arabidopsis COPII components, AtSec24B and AtSec24C, is essential for male and female gametogenesis. Planta **238:** 561–575

Vidali L, Augustine RC, Kleinman KP, Bezanilla M (2007) Profilin is essential for tip growth in the moss Physcomitrella patens. Plant Cell **19:** 3705–3722

Vidali L, van Gisbergen PAC, Guérin C, Franco P, Li M, Burkart GM, Augustine RC, Blanchoin L, Bezanilla M (2009) Rapid formin-mediated actin-filament elongation is essential for polarized plant cell growth. Proc Natl Acad Sci USA **106:** 13341–13346

Viotti C, Krüger F, Krebs M, Neubert C, Fink F, Lupanga U, Scheuring D, Boutté Y, Frescatada-Rosa M, Wolfenstetter S, et al. (2013). The endoplasmic reticulum is the main membrane source for biogenesis of the lytic vacuole in *Arabidopsis*. Plant Cell **25:** 3434–3449

Wang X, Chung KP, Lin W, Jiang L (2017). Protein secretion in plants: conventional and unconventional pathways and new techniques. J Exp Bot **69:** 21–37

Whittle JRR, Schwartz TU (2010) Structure of the Sec13–Sec16 edge element, a template for assembly of the COPII vesicle coat. J Cell Biol **190:** 347–361

Wu S-Z, Bezanilla M (2014) Myosin VIII associates with microtubule ends and together with actin plays a role in guiding plant cell division. eLife Sci **3:** e03498

Wu S-Z, Yamada M, Mallett DR, Bezanilla M (2018) Cytoskeletal discoveries in the plant lineage using the moss Physcomitrella patens. Biophys Rev **10:** 1683–1693

Zeng Y, Chung KP, Li B, Lai CM, Lam SK, Wang X, Cui Y, Gao C, Luo M, Wong K-B, et al. (2015). Unique COPII component AtSar1a/AtSec23a pair is required for the distinct function of protein ER export in *Arabidopsis thaliana*. Proc Natl Acad Sci USA **112:** 14360–14365

Zeng Y, Li B, Ji C, Feng L, Niu F, Deng C, Chen S, Lin Y, Cheung KCP, Shen J, et al. (2021) A unique AtSar1D-AtRabD2a nexus modulates autophagosome biogenesis in Arabidopsis thaliana. Proc Natl Acad Sci USA **118**

Zhang H, Zhang L, Gao B, Fan H, Jin J, Botella MA, Jiang L, Lin J (2011) Golgi apparatus-localized synaptotagmin 2 is required for unconventional secretion in Arabidopsis. PLoS ONE **6:** e26477